Efficient and Tunable Photoinduced Honeycomb Lattice in an Atomic Ensemble

Feng Wen, Xun Zhang, Huapeng Ye, Wei Wang, Hongxing Wang, Yanpeng Zhang, Zhiping Dai, and Cheng-Wei Qiu**

Artificial periodic structures (APS) with controllable optical properties are highly demanded in all-optical devices and circuits in communication networks. However, APS realized in solid materials are usually non-tunable and inherently possess immutable photonic bandgap. In this article, a novel honeycomb lattice in an atomic ensemble by utilizing the multi-beam interference method is reported. Unlike the honeycomb lattice formed in solid materials, the optical properties of this photoinduced honeycomb lattice, such as the absorption/dispersion coefficients and the photonic bandgap can be efficiently tuned by two-photon detuning and Rabi frequency, resulting in both amplitude- and phase- type honeycomb lattice. Based on the two-photon quantum-imaging method, the near-field diffraction of the honeycomb lattice is also investigated. It is found that the resolution of the diffraction pattern is tunable by simply adjusting the manner of the two detectors scanning across the imaging beams. In addition, the contrast of the pattern can be greatly enhanced by tuning the optical properties of the lattice. Such an optical honeycomb lattice with tunable properties could find applications in all-optical switching at the few photons level and paves the way for the generation and manipulation of optical topological insulators.

1. Introduction

Artificial periodic structures (APS) such as waveguide arrays,[1,2] photonic crystals,[3–5] and metamaterials,[6,7] have attracted substantial attention in the past several years due to their unprecedented capacities in light manipulation ranging from strong slow light,[8] inhibited spontaneous emission,[9] photon–atom bound states,[10] vortex beams, and orbital angular momentum,[11–14] to all-optical signal processing and switching.[15–17] APS can be fabricated into various geometries, among which the honeycomb lattices are known to support larger bandgaps, and help to strongly modify or even suppress the propagation direction of light at desired frequencies. Furthermore, the honeycomb lattice also exhibits certain graphene-like properties naturally and was suggested to prepare the photonic topological insulators,[18–22] in which the propagating light beams are confined at the edges without scattering energy into the bulk, and robust against defects. Conventionally, two methods, namely the femtosecond laser writing technique and the optically induced method, are utilized to fabricate the honeycomb lattices. The former method is valid only in solid materials, while the latter can be used in both solid and gaseous materials. So far, the honeycomb lattices in solid materials are widely investigated;[23,24] nevertheless, the refractive index of the resulting periodic structures in solid materials is usually non-tunable, and thus leading to immutable photonic bandgap (PBG), such as photonic crystals with fixed periodic structures.[25] APS with tunable optical properties are highly demanded in all-optical devices and circuits in communication networks. It would be of great importance if we can obtain some degree of tunability in the photonic band structure.[26,27] One possibility to tune the optical properties is demonstrated in filtrated liquid crystals.[25] Nevertheless, the modulation efficiency with liquid crystals is limited by the long relaxation time in the

Dr. F. Wen, Dr. X. Zhang, Dr. W. Wang, Prof. H. Wang, Prof. Y. Zhang
Key Laboratory for Physical Electronics and Devices of the Ministry of Education & School of Science & Shaanxi Key Lab of Information Photonic Technique & Institute of Wide Bandgap Semiconductors
Xi'an Jiaotong University
Xi'an, 710049 P.R. China

Dr. F. Wen, H. Ye, Prof. Z. Dai, Prof. C.-W. Qiu
Department of Electrical and Computer Engineering
National University of Singapore
4 Engineering Drive 3, 117583 Singapore
E-mail: hydzp@hynu.edu.cn; eleqc@nus.edu.sg

DOI: 10.1002/lpor.201800050

Prof. Z. Dai
College of Physics and Electronic Engineering
Hengyang Normal University
Hengyang, 421002, China

H. Ye
Guangdong Provincial Key Laboratory of Optical Information Materials and Technology & Institute of Electronic Paper Displays
South China Academy of Advanced Optoelectronics
South China Normal University
Guangzhou, 510006, China

H. Ye
National Center for International Research on Green Optoelectronics
South China Normal University
Guangzhou, 510006, China

process of molecular reorientation which is usually based on slow electro- and thermo-optics effects. Indeed, tuning the optical properties directly by optical means is more desirable. This can be achieved in the so-called electromagnetically induced grating (EIG) system, and the tunable transmission spectra is demonstrated both in cold[28] and hot[29] atomic samples. Unlike traditional APS in solid materials, such periodic structure is created by interfering two laser beams, and consequently the resulting photonic structure is highly tunable.[30,31] So in this paper, we report a novel honeycomb lattice in an ultra-cold atomic ensemble, where the periodic refractive index can be dynamically modulated by the all-optical method. In particular, we consider first the absorption/dispersion coefficients, the PBG structure, and transmission of the optically induced honeycomb lattice, and demonstrate that those properties can be modulated significantly by two-photon detuning and Rabi frequency. Using two-photon quantum-imaging method, we considered the near-field diffraction pattern of the honeycomb lattice, and found that the resolution of the diffraction pattern can be efficiently tuned by simply adjusting the manner of the two detectors scanning across the imaging beams. In addition, we also show that the contrast of the diffraction pattern can be greatly enhanced by tuning the optical property of such photoinduced nonmaterial lattice. It may open up the possibility of generating a honeycomb lattice in atomic vapors under physical mechanisms that are vastly different from those in solid-state materials.

It is worth mentioning that our scheme has the following advantages. First, the optical lattice written in an atomic assemble is reconfigurable and can be dynamically tuned. So the absorption/dispersion index and the PBG structures of the induced honeycomb lattice can be dynamically modulated by adjusting the two-photon detuning and Rabi frequency. Second, other complex lattice structures, that is, quasi-crystals, square lattice, kagome lattice, defect-mediated lattice, Bessel lattice, virtual lattice, ring lattice, and 3D photonic lattice, can also be realized by using the multi-beam interference method in current systems. Third, the formation of lattice, as well as the tuning, is all done all-optically. Optical lattice structures both in the cold and warm atomic systems are quite stable, so long as the lattice forming beams are stable. This provides an effective way for creating photonic topological insulators.

2. Optical Properties of Honeycomb Lattice

We start by considering a typical electromagnetically induced transparency (EIT) system confined in a regular cold magneto optical trap (MOT). As shown in **Figure 1**a, the EIT system is composed by the interaction between an ensemble of cascade-type three-level cold atoms[32] and four continuous wave lasers, including a weak field E_P and a lattice-forming field $E_{\text{eff}}(x, y)$. Here, the lattice-forming field is generated by interfering the three ordinarily polarized plane waves with the same frequency ω_S. To be specific, the three plane waves, being symmetrically placed with respect to z, are launched into the cold atomic ensemble at an angle of $2\pi/3$ between each other, as shown in Figure 1a. The effective Rabi frequency of $E_{\text{eff}}(x, y)$ can be written as $\Omega_{\text{eff}} = \sum_{m=1}^{3} \Omega_S \exp[i k_0 \overrightarrow{b_m} \bullet \overrightarrow{r}]$, where $\overrightarrow{b_1} = (1, 0), \overrightarrow{b_2} = (-1/2, \sqrt{3}/2)$, and $\overrightarrow{b_3} = (-1/2, -\sqrt{3}/2)$. $k_0 = 4\pi/3a$, with a period along the x-axis, and $\Omega_S = \mu_{10} E_2/\hbar$ represents the Rabi frequency of the coupling fields. The corresponding intensity distribution of $E_{\text{eff}}(x, y)$ is shown in **Figure 2**a, where the optically induced interference pattern possesses a 2D honeycomb lattice with a threefold symmetry.

As usual, the weak field E_P with Rabi frequency Ω_P is used to probe the atomic transition $|0\rangle \rightarrow |1\rangle$, being detuned with $\Delta_1 = \omega_P - \omega_{10}$, while the lattice-forming field $E_{\text{eff}}(x, y)$ (with effect Rabi frequency $\Omega_{\text{eff}}(x, y)$) originating from the same laser is coherently coupled with the levels $|1\rangle$ and $|2\rangle$, being detuned with $\Delta_2 = \omega_S - \omega_{21}$. This results in an EIT if $\Delta_1 + \Delta_2 = 0$ and $\Omega_P \ll \Omega_{\text{eff}}(x, y)$. As the atomic transition channel $|1\rangle \rightarrow |2\rangle$ is periodically dressed by $E_{\text{eff}}(x, y)$, according to the dressed state theory analysis, the $|1\rangle$ will be split into dressed states $|+\rangle$ and $|-\rangle$ with eigenvalues $\lambda_{\pm} = \Delta_2/2 \pm (\Delta_2^2/4 + |\Omega_{\text{eff}}(x, y)|^2)^{1/2}$. Consequently, the spatial distribution of the dressed state $|+\rangle$ and $|-\rangle$ also exhibits honeycomb lattice since the spatial intensity distribution of $\Omega_{\text{eff}}(x, y)$ presents a honeycomb lattice, as shown in Figure 1b and the panels Figure 1c1,c2.

The optical response of the cold atomic ensemble to probe fields is governed by the master equation $\partial\rho/\partial t = -i/\hbar[\rho, H_{\text{int}}]$,[33] here, $H_{\text{int}} = \Omega_P e^{-i\Delta_1 t}|0\rangle\langle 1| + \Omega_{\text{eff}} e^{-i\Delta_2 t}|1\rangle\langle 2| + h.c$ denotes the atom–field interactions Hamiltonian. Δ_1 and Δ_2 describe the single-photon detuning of E_P and $E_{eff}(x, y)$ from the atomic channel $|0\rangle \rightarrow |1\rangle$ and $|1\rangle \rightarrow |2\rangle$, respectively, with $\omega_{mn} = \omega_m - \omega_n$ $(m, n = 0, 1, 2)$. Solving the master equation under the rotating-wave approximation and assuming that the system is initially in its ground state $|0\rangle$ (more details can be found in Supporting Information), the polarization at ω_P takes the form $P(\omega_P) = \varepsilon_0 \chi(\omega_P) E_P(\omega_P)$, where the steady state of the optical-induced susceptibility is

$$\chi = \frac{i N|\mu_{10}|^2}{\hbar\varepsilon_0} \frac{d_{20}}{d_{10}d_{20} + |\Omega_{eff}|^2} \tag{1}$$

where N is the density of the atomic ensemble, ε_0 the vacuum permittivity, μ_{10} the electric dipole moment, $d_{10} = \gamma_{10} + i\Delta_1$ and $d_{20} = \gamma_{20} + i(\Delta_1 + \Delta_2)$ the complex decay rates, describing single- and two-photon detuning, respectively, and γ_{ij} the dephasing rate between $|i\rangle$ and $|j\rangle$.

As indicated by Equation (1), the optical response of the atomic ensemble to the probe field will be modulated periodically with a honeycomb profile due to the spatial distribution of the dressed state $|\pm\rangle$ exhibiting a honeycomb lattice. To illustrate this point explicitly, the optical-induced susceptibility χ to the probe fields at lattice sites and the regions immediately around the sites is plotted in Figure 2b1,b2 for comparison. From the absorption curve (solid lines in Figure 2b1,b2), we find that the probe field is quite opaque at lattice sites and almost transparent at the regions immediately around the lattice sites. This leads to a substantial amplitude modulation across the probe beam. On the other hand, the dispersion within the EIT window (dashed lines in Figure 2b1,b2) is positive at lattice sites but negative at the regions immediately around it. Therefore, a large phase modulation across the probe beam can be achieved if the probe field passes through the EIT system. As the absorption and dispersion coefficients of the probe field are highly dependent on $E_{eff}(x, y)$, they are

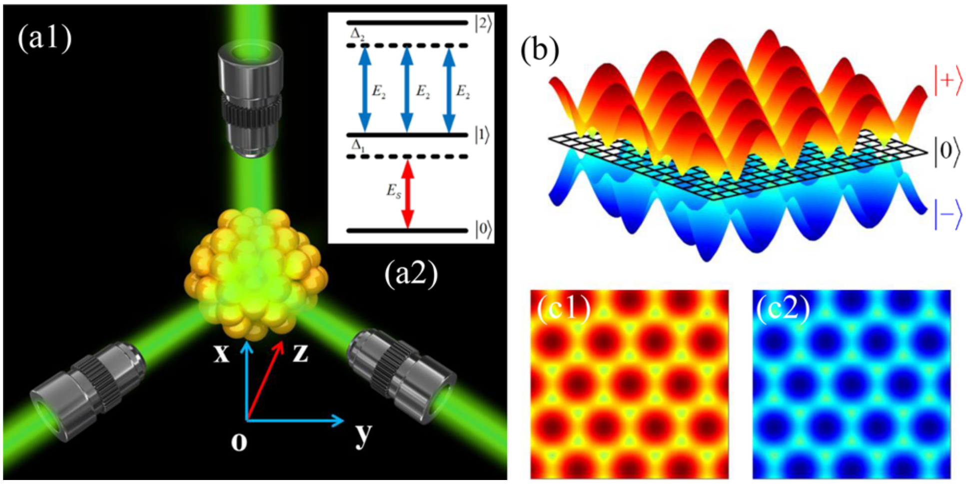

Figure 1. Schematic of the honeycomb lattice in an atomic ensemble: a1) cascade-type three-level scheme with $|0\rangle$ ($5S_{1/2}(F = 3)$), $|1\rangle$ ($5P_{3/2}(F = 3)$), and $|3\rangle$ ($5D_{5/2}$) of ^{85}Rb atoms,[32] interacting with a probe field and the lattice-forming fields, and a2) the corresponding geometry of lattice-forming fields upon the cold atoms ensemble. b) Energy level splitting due to the three beam interference pattern with $\Delta_2 = 0$. c1,c2) The top views of the two split sublevels $|+\rangle$ and $|-\rangle$, respectively.

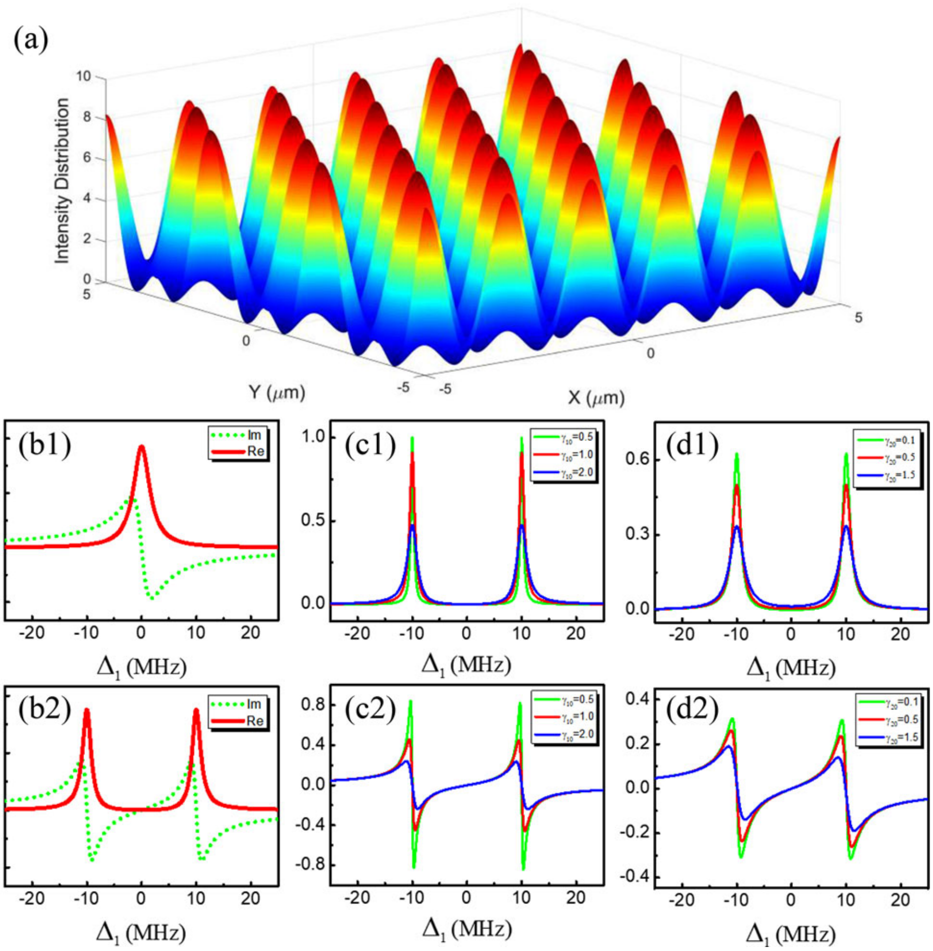

Figure 2. a) Spatial distribution of the lattice-forming laser. The absorption spectrum and dispersion spectrum of atomic ensemble at b1) nodes and b2) anti-nodes of the lattice-forming laser. c1) Probe absorption spectrum and c2) dispersion spectrum at anti-nodes with $\gamma_{20} = 0.1$ MHz for various dephasing rate γ_{10} from 0.1, 0.5, to 2.0 MHz. d1) Probe absorption spectrum and d2) dispersion spectrum at anti-nodes with $\gamma_{10} = 1$ MHz for various dephasing rate γ_{20} from 0.1, 0.5, to 1.5 MHz. Other parameters are $a = 2$ μm, and $\Omega_{\text{eff}} = 6$ MHz.

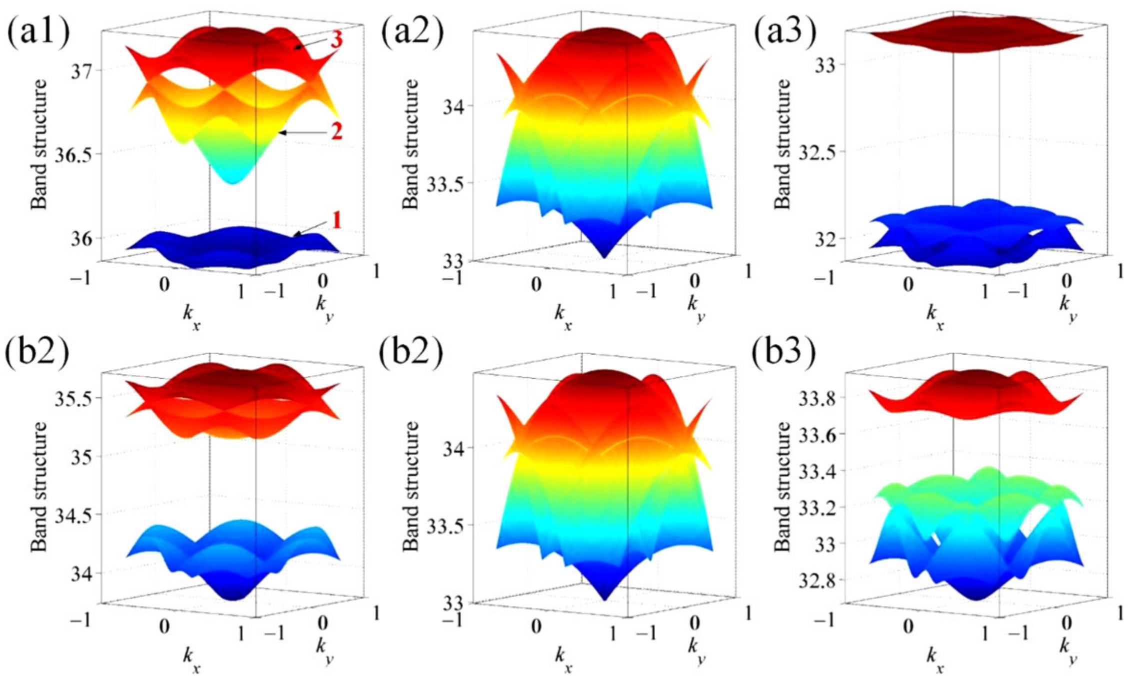

Figure 3. a1–a3) and b1–b3) The first three photonic band structures of honeycomb lattice corresponding to $\Omega_{\text{eff}} = 6$ MHz and $\Omega_{eff} = 12$ MHz, respectively, with a1) and b1) $\Delta_1 = -\Delta_2 = -3$, a2) and b2) $\Delta_1 = \Delta_2 = 0$, and a3) and b3) $\Delta_1 = -\Delta_2 = 3$. Other parameters are $\gamma_{10} = 1$ MHz, $\gamma_{20} = 0.1$ MHz, and $a = 2$ µm.

expected to change periodically when the lattice-forming laser changes from lattice sites to the regions immediately around the sites across x-axis and y-axis, and consequently the 2D honeycomb periodical amplitude and phase modulation will be realized in this atomic ensemble. The absorption and dispersion spectra for various dephasing rates γ_{10} and γ_{20} are shown in Figure 2c,d. It can be clearly seen that the width of EIT resonance (transparency dip) in the absorption spectrum becomes deeper until it forms a transparency window when γ_{10} and γ_{20} change from higher dephasing rates to lower dephasing rates, see Figure 2c1,d1. Meanwhile, the variation of dispersion at the transparency region is insensitive as the dephasing rate changes. Compared with γ_{10}, however, a steeper dispersion at the transparency region is obtained if γ_{20} changes, see Figure 2c2,d2.

It is worth mentioning that a typically photonic band-gap is created simultaneously in our scheme. Based on the plane wave expansion method, we analyze the photonic band gap (PBG) structure of the honeycomb lattice by tuning the two-photon detuning and Rabi frequency of the lattice-forming field, where all the important parameters can be taken into account with this method. In each panel of **Figure 3**, we display the lowest three PBG bands in the first Brillouin zone. It clearly exhibits that the PBG structures of the lattice are sensitive to the two-photon detuning and Rabi frequency being adjusted. We first consider the influence of the two-photon detuning on the band structure by fixing the $\Omega_{\text{eff}} = 6$ MHz, as shown in Figure 3a1–a3. Specifically, if $\Delta_1 = \Delta_2 = 0$ MHz, the honeycomb lattice is homogeneous as the phase modulation is absent, and the corresponding PBG structure is shown in Figure 3a2, where the edges of the upper two bands merge with each other and there are no Dirac cones in the PBG. By setting $\Delta_1 = -\Delta_2 = -3$ MHz, see Figure 3a1, we can see that there are six points and cones between the upper two bands (the bands 2 and 3 marked in Figure 3a1) at the corners of the first Brillouin zone, and the dispersion relation is linear around the Dirac points. However, the PBG structure is quite different from those in Figure 3a1 if $\Delta_1 = -\Delta_2 = 3$ MHz. A big band gap opens between the upper two bands and the six Dirac cones in the original PBG disappeared. Nevertheless, one can find that there are 6 Dirac points between bands 1 and 2, as shown in Figure 3a3. The influence of two-photon detuning on the PBG structure with increased $\Omega_{\text{eff}} = 12$ MHz is presented in Figure 3b1–b3. Compared with Figure 3a1,b1, one can see that the upper two bands in Figure 3b1 become almost degenerate and flat, and the opened gap between the bands 1 and 2 is smaller in Figure 3a1. However, the PBG structures shown in Figure 3a2 are quite the same as Figure 3b2. Therefore, the PBG structures can be easily modulated by choosing the parameter regions, which is one of the main advantages of the current system.

Since PBG will affect the transmission/reflection of the probe beam uniformly and does not lead to the diffraction in the transverse directions, we only consider the lattice in the transverse direction in the following. Next, we explore the propagation dynamics of the probe field within the honeycomb lattice, which can be expressed via a self-consistent equation, with the induced polarizations serving as the driving source,

$$\frac{\partial E_P}{\partial z} = (-m(x, y)/2 + in(x, y))\, E_P \qquad (2)$$

where $m(x, y) = (4\pi/\lambda)\mathrm{Im}[\chi(\omega_P)]$ and $n(x, y)L = (2\pi L/\lambda)\, Re[\chi(\omega_P)]$ are the two-photon absorption and the

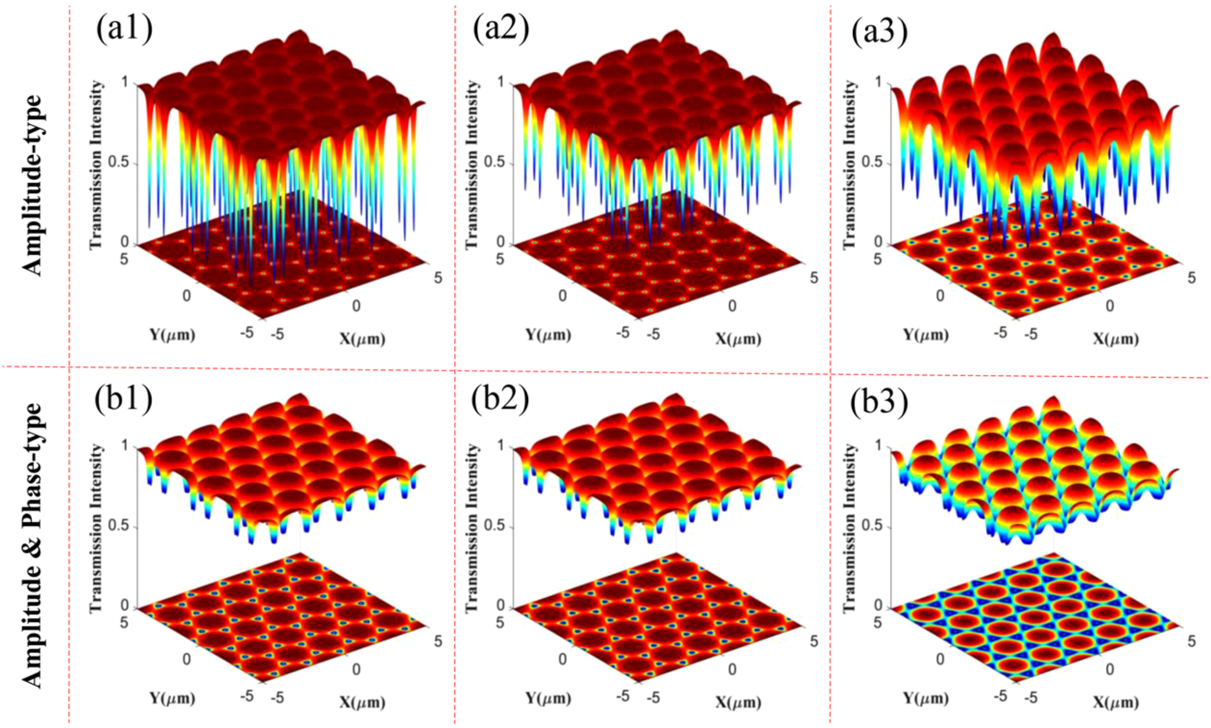

Figure 4. The output profile of the transmission function $T(x, y)$ plotted over four space periods along x and y. a) The amplitude honeycomb lattice by setting $\Delta_1 = \Delta_2 = 0$MHz, with a1) $\gamma_{10} = 0.5$, $\gamma_{20} = 0.1$MHz, a2) $\gamma_{10} = 1$, $\gamma_{20} = 0.1$MHz, a3) $\gamma_{10} = 1$, $\gamma_{20} = 0.5$ MHz, under the same color scale. b) The hybrid honeycomb lattice by setting$\Delta_1 = -\Delta_2 = 3$ MHz, with b1) $\gamma_{10} = 0.5$, $\gamma_{20} = 0.1$MHz, b2) $\gamma_{10} = 1$, $\gamma_{20} = 0.1$MHz, b3) $\gamma_{10} = 1$, $\gamma_{20} = 0.5$ MHz, under the same color scale. Other parameters are $a = 2$ μm and $\Omega_{\text{eff}} = 6$ MHz.

phase shift coefficient to the probe field, respectively. Equation (2) can be solved analytically, and the normalized transmission function with interaction length L is obtained as

$$T(x, y) = \exp\left[-\frac{m(x, y)L}{2} + in(x, y)L\right] \tag{3}$$

Figure 4a1–a3 illustrate the transmission profiles of the probe beam at the output surface of atomic ensemble by setting $\Delta_1 = \Delta_2 = 0$ MHz for various dephasing rates, as displayed in the caption. It can be clearly seen from Figure 4a1 that the probe beam is significantly absorbed at the lattice sites but much less at the regions immediately around the sites. Recall that the intensity of the lattice-forming field is very weak at the six lattice sites, whereas strong enough at the regions immediately around the sites. This implies that the probe beam at the six lattice sites is absorbed according to the usual Beer law, and much less in the regions immediately around the lattice sites due to the dressing effect. In other words, the transmission profile of the probe field is 2D intensity-dependent, and thus a phenomenon reminiscent of amplitude-type honeycomb lattice is realized, as shown in the bottom of Figure 4a1. The absorption spectrum decreased significantly if $\gamma_{10} = 1$ (see Figure 2c1), and thus leading to the reduction of the transmission profile, as shown in Figure 4a2. It is worth mentioning that the absorption spectrum is insensitive to the increase of γ_{20} (see Figure 2d1). Therefore, as shown in Figure 4a3, the intensity change of the transmission profile is not obvious. On the other hand, Figure 4b1 shows the transmission function $T(x, y)$ over several periods by setting $\Delta_1 = -\Delta_2 = 3$ MHz. In this case, the probe field experiences a rapid phase change at the lattice sites due to the newly introduced phase modulation, and then a phase modulation is imposed onto its transmission profile. Accordingly, a spatial hybrid honeycomb lattice (both amplitude and phase modulation) is achieved in this case, as shown in the bottom of Figure 4b1. The variation of the dispersion at $\Delta_1 = -\Delta_2 = 3$ can be ignored even if γ_{10} is varying from 0.5 to 1 MHz (see Figure 4c2). Hence, the transmission profile in Figure 4b2 is almost the same as in Figure 4b1. Nevertheless, a steeper dispersion is obtained if γ_{20} changes from 0.1 to 0.5 MHz (see Figure 2d2), and then a more rapid phase change can be observed in the transmission profile, as shown in Figure 4b1.

3. Two-Photon Near-Field Diffraction Pattern of the Honeycomb Lattice

It is shown that the optical transmission property as well as the PBG structure of the honeycomb lattice can be effectively controlled by the special tuning of the laser field intensities and detuning. In the following sections, we will further explore the feature of the honeycomb lattice from the aspect of the near-field diffraction phenomenon by introducing the two-photon quantum-imaging configuration. For convenience, we assume that the entangled photon pairs generated from SPDC have the

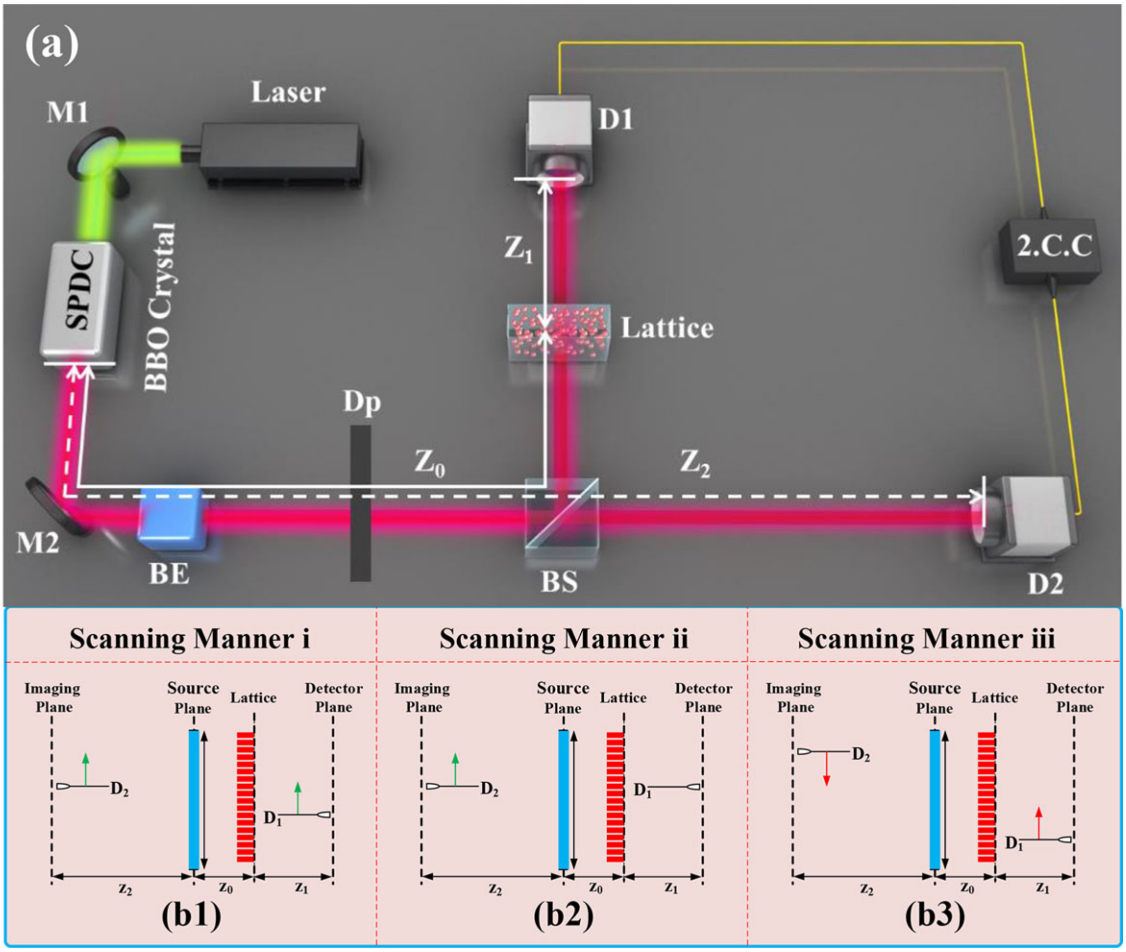

Figure 5. a) Diagram for two-photon quantum imaging. BE, beam expander; Dp, diaphragm; M1 and M2, mirrors; BS, beam splitter; 2.C.C, second-order coincidence counting; D1, bucket detector; D2, single-photon detector. b1–b3) The three special scanning ways of two single-photon detectors across the signal and the idler beams.

same wavelength $\lambda_s = \lambda_i = 780.2$ nm, and period along the x-axis a 2 μm.

As shown in **Figure 5**, within the Beta barium borate (BBO) crystal cut for type-I phase matching, a pair of spatially entangled photons (signal and idler photon) are generated through the spontaneous parametric down-conversion (SPDC) process. They are first separated by a beam splitter (BS), and then propagated along two different routes, namely the signal arm and idler arm. In the signal arm, the EIT system with honeycomb lattice structure is placed between BS and bucket detector D_1, and the signal photons are coupled with the EIT system via atomic channel $|0\rangle \rightarrow |1\rangle$ and collected by a bucket detector D_1. Meanwhile, in the idler arm, the idler photon is employed as a trigger and detected by the reference detector D_2, where the coincidence counting is taken. Here, the distances from the BBO crystal to atomic ensemble and the reference detector D_2 are z_0 and z_2, respectively. The distance between the atomic ensemble and bucket detector D_1 is z_1.

According to Glauber's quantum measurement theory,[34] the second-order coincidence counting rate for two-photon quantum-imaging can be expressed as

$$C = \frac{1}{P}\int_0^P\int_0^P dt_1 dt_2 \langle \Phi | E^{(-)}(\vec{\kappa_1}, t_1) E^{(-)}(\vec{\kappa_2}, t_2) E^{(+)} \times (\vec{\kappa_2^*}, t_2) E^{(+)}(\vec{\kappa_1^*}, t_1) | \Phi \rangle \tag{4}$$

where $|\Phi\rangle$ the biphoton state function at output surface of the BBO crystal, takes the form $\int d\omega_i \int d\omega_s \int d^2\vec{\rho_1} \int d^2\vec{\rho_2} \delta(\omega_i + \omega_s - \omega_0)\delta(\vec{\rho_1} + \vec{\rho_2})|1_{k_i}, 1_{k_s}\rangle$[35], with ω_m, $\vec{\rho_m}$ and k_m $(m = s, i)$ being the angular frequency, transverse coordinate, and wave vectors of entangled photon, respectively. The terms $\delta(\omega_i + \omega_s - \omega_0)$ and $\delta(\vec{\rho_1} + \vec{\rho_2})$ in $|\Phi\rangle$ ensure that the biphoton generated from SPDC are entangled both in frequency and spatial domain, respectively. $E^{(+)}(\vec{\kappa_i}, t_i)(E^{(-)}(\vec{\kappa_i}, t_i))$ is the positive (negative) part of $E(\vec{\kappa_i}, t_i)$ $(i = 1, 2)$. $\vec{\kappa_i}$ is the transverse coordinate and t_i is the triggering time, in ith detection plane. P is chosen to be the capture of the coincidence count.

We begin by computing the field at the detector in terms of the photon destruction operators at the output surface of the crystal. Taking the propagation effect into account, the wave function that describes the propagation of each mode of angular frequency ω_k from output surface of the BBO crystal to the transverse point of detectors should be rewritten as $E^{(+)}(\overrightarrow{\kappa_k}, t_k) = \int d\omega_k \int d^2\overrightarrow{\rho_k}\, \Xi_k g(\omega_k) e^{-i\omega_k t_k} h_k(\omega_k, \overrightarrow{\rho_k}, \overrightarrow{\kappa_k}) a_k(\overrightarrow{\rho_k}, \omega_k) (k = 1, 2)$, where $h_k(\omega_k, \overrightarrow{\rho_k}, \overrightarrow{\kappa_k})$ describes the propagating mode ω_k from output surface of crystal $\overrightarrow{\rho_k}$ to the detector with transverse point $\overrightarrow{\kappa_k}$, $g(\omega_k)$ is the narrow bandwidth of filter function peaked with central frequency Ω_k ($\omega_k = \Omega_k + \upsilon_k$ and $\upsilon_k \leq \Omega_k$), and $\Xi_k = \sqrt{\hbar\omega_k/2\varepsilon_0}\; a_k(\overrightarrow{\rho_k}, \omega_k)$ is the photon annihilation operator, satisfying $[a(\overrightarrow{\rho}, \omega_i), a^+(\overrightarrow{\rho'}, \omega')] = \delta(\overrightarrow{\rho} - \overrightarrow{\rho'})\delta(\omega - \omega')$. Assuming that the paraxial approximation is always held,[36–38] the impulse response functions for the idler arm and the signal arm become $h_2(\overrightarrow{\rho_2}, \overrightarrow{\kappa_2}) \propto \exp[\frac{i\omega_i z_2}{c}] \exp[\frac{i\omega_i}{2cz_2}(\overrightarrow{\rho_2} - \overrightarrow{\kappa_2})^2 + i\overrightarrow{\rho_2} * \overrightarrow{k_i}]$ and $h_1(\overrightarrow{\rho_1}, \overrightarrow{\kappa_1}) \propto -\frac{i\omega_s}{2\pi c z_1} \exp[\frac{i\omega_s z_1}{c}] \int d^2\overrightarrow{\eta}\, T(\overrightarrow{\eta}) \exp[\frac{i\omega_s}{2cz_0}(\overrightarrow{\rho_1} - \overrightarrow{\eta})^2 \exp[\frac{i\omega_s}{2cz_1}(\overrightarrow{\eta} - \overrightarrow{\kappa_1})^2 + i\overrightarrow{\rho_1} * \overrightarrow{k_s}]$, respectively.

Substituting $h_1(\overrightarrow{\rho_1}, \overrightarrow{\kappa_1})$, $h_2(\overrightarrow{\rho_2}, \overrightarrow{\kappa_2})$, and $T(x, y)$ into $\Psi(\kappa_1, \kappa_2) = \langle 0| E^{(+)}(\overrightarrow{\kappa_2^*}, t_2) E^{(+)}(\overrightarrow{\kappa_1^*}, t_1)|\Phi\rangle$ and completing the integration on transverse mode $\overrightarrow{\rho_k}$, the two-photon amplitude is obtained

$$\Psi(\kappa_1, \kappa_2) = A_0 \int d^2\overrightarrow{\eta}\, T(\overrightarrow{\eta}) \exp\left[-\frac{i\omega_s}{c}\overrightarrow{\eta} * \left(\frac{\overrightarrow{\kappa_1}}{z_1} + \frac{\overrightarrow{\kappa_1}}{z_0 + z_2}\right)\right] \times \exp\left[\frac{i\omega_s}{2c}\overrightarrow{\eta} * \left(\frac{1}{z_1} + \frac{1}{z_0 + z_2}\right)\right] \tag{5}$$

where the irrelevant terms are absorbed into A_0, and $\overrightarrow{\eta}$, $\overrightarrow{\kappa_1}$, and $\overrightarrow{\kappa_2}$ are the transverse coordinates at the atomic ensemble, D_1, and D_2, respectively. On the other hand, $T(x, y)$ can be expanded into 2D Fourier series as

$$T(x, y) = \sum_{m,n=-\infty}^{\infty} C_{mn} \exp\left[i2\pi\left(\frac{m}{a}x + \frac{n}{\sqrt{3}a}y\right)\right] \tag{6}$$

where a is the least distance between any two adjacent lattice sites, and C_{mn} is 2D Fourier coefficient. Finally, substituting Equation (6) into Equation (5) and then completing the integration on $\overrightarrow{\eta}$, the biphoton amplitude can be simplified as

$$\begin{aligned}\Psi(u_1, u_2; v_1, v_2) &= C_0 \sum_{m,n=-\infty}^{\infty} c_{mn}\left\{\exp\left[-i\pi\lambda_s\frac{z_1(z_0+z_2)}{z_1 + z_0+z_2}\left(\frac{m^2}{a^2} + \frac{n^2}{3a^2}\right)\right]\right.\\ &\left.\times \exp\left[i\frac{2\pi m}{a}\frac{(z_0+z_2)u_1 + z_1 u_2}{z_1 + z_0+z_2}\right]\exp\left[i\frac{2\pi n}{\sqrt{3}a}\frac{(z_0+z_2)v_1 + z_1 v_2}{z_1 + z_0+z_2}\right]\right\}\end{aligned} \tag{7}$$

where (u_k,v_k) $(k = 1, 2)$ are coordinates (X, Y) in D_k detection planes, respectively. Careful examination of Equation (7) reveals that the two-photon diffraction pattern of the honeycomb lattices is determined not only by the intrinsic optical properties of the honeycomb lattices, which can be effectively controlled via selecting a special parameter region, but by the scanning manners of two detectors across the signal and idler beams as well. Some interesting conclusions can be predicted immediately based on Equation (7). First, the optical properties of the honeycomb lattices, that is, amplitude/phase, are contained in C_{mn}, through which the improvement about the visibility as well as the signal-to-noise ratio of the diffraction pattern may be implemented. Second, the first exponential term in Equation (7), referred to as "localization" term, describes the phase change of the diffraction orders along the propagation directions, and determines whether self-imaging occurs or not. For the ideal plane-wave illumination, the self-images repeat at multiples of the Talbot length, $z_T = 3a^2/2\lambda_P$. Third, the magnification of lattice is closely dependent on the scanning manner of two detectors across the signal and the idler beams. Generally, three special scanning ways are included: i) Both detectors are scanned synchronously across the signal and idler beams with identical directions (see Figure 5b1), that is, guaranteeing $u_1 = u_2$ and $v_1 = v_2$, and the corresponding magnification M_1 factor is always equal to 1 when D_2 is scanned along the diffraction direction. ii) One of these detectors is fixed at its origin while the other is moved along x- and y-axes (see Figure 5b2). Compared with the original lattice, the self-imaging is magnified by a factor $M_2 = 1 + z_1/(z_0+z_2)$. iii) Both detectors are scanned synchronously across the two beams but in opposite directions (see Figure 5b3), that is, $u_1 = -u_2$ and $v_1 = -v_2$, and the corresponding magnification is $M_3 = 1 + 2z_1/(z_0+z_2 - z_1)$. Therefore, the two-photon diffraction pattern of the lattices can be modulated arbitrarily in case of ii) and iii).

Figure 6 shows the numerically computed near-field diffraction pattern of the honeycomb lattice under the resonant interaction circumstance, that is, $\Delta_1 = \Delta_2 = 0$ MHz, with selecting the first manner i). We see from Figure 6a,b that a typical self-imaging of honeycomb lattice is produced, where both the transverse and longitudinal resolutions of the diffraction patterns remain unchanged when D_2 is scanned along the diffraction direction z. In other words, the periods of the diffraction patterns are all equal to the original honeycomb lattice. This interesting phenomenon is attributed to the fact that the amplification factor M_1 is always equal to 1 if D_2 is scanned along the z-direction, and thus the transverse and the longitudinal sizes of diffraction patterns are independent of the positions of D_2. To illustrate it more intuitively, in Figure 6c1–c4, we also display the 2D diffraction patterns separately at the factional Talbot length $z_2 = 0, z_T/3$, $z_T/2$, and z_T, respectively. Specifically, we first investigate the diffraction patterns on the X-Y plane when D_2 is fixed at $z_2 = 0$. As shown in Figure 6c1, the pattern shows that the intensity distribution at lattice sites is higher than that in the regions immediately around the lattice sites, and the period of the pattern is exactly equal to that of the original lattice. Therefore, the six lattice sites resemble the honeycomb lattice. Next, we focus on the imaging at 1/3 Talbot plane. As depicted in Figure 6c2, the intensity distribution resembles a new honeycomb array with a reduced period equal to $3 \times 3^{1/2}$ µm, and the basis vectors of the imaging lattice are rotated by an angle of 30° with respect to the original lattice. In addition, a careful examination of Figure 6c2 further reveals that the honeycomb centers have high intensity and the six lattice sites have low intensity. This is because the nearest two spots partially overlap and consequently cause the fields from corresponding spots to interfere partially, and thus the six bright spots evolve into the dark spots. Different from

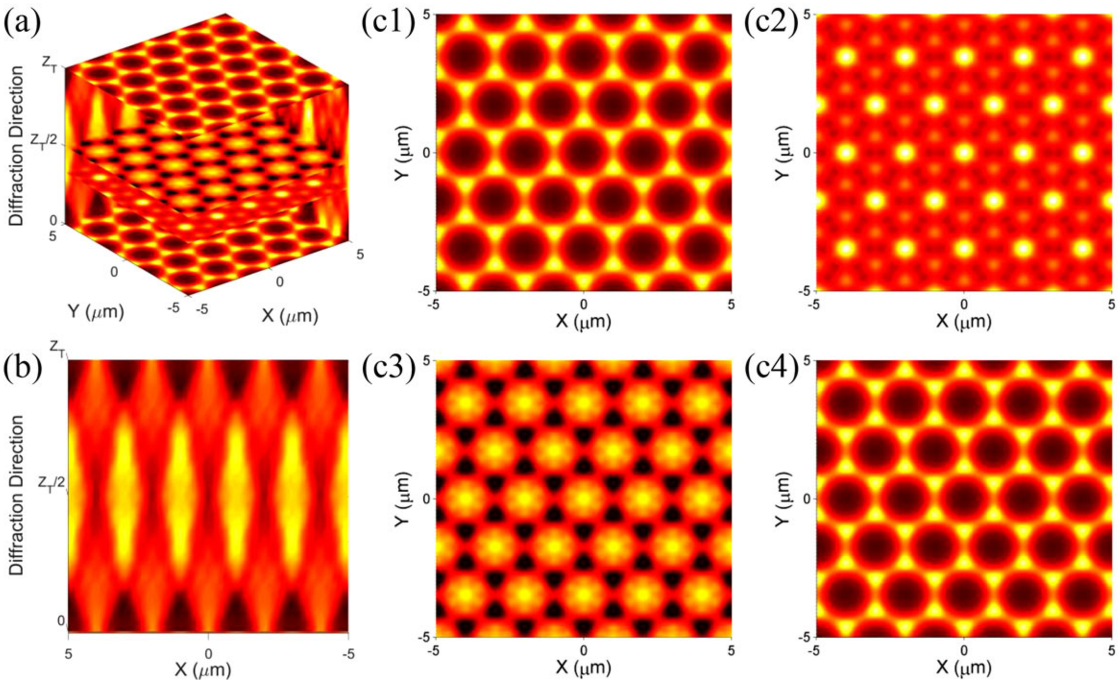

Figure 6. a) The near-field diffraction pattern of 2D honeycomb lattice along the z-direction obtained by scanning D_1 and D_2 in manner i), with setting $\Delta_1 = \Delta_2 = 0$ MHz. b) Self-imaging carpets at $y = 0$ parallel to X-Z plane. c) Contour plots the self-imaging parallel to X-Y plane at c1) 0, c2) $z_T/3$, c3) $z_T/2$, and c4) z_T, respectively. Other parameters are $\gamma_{10} = 1$ MHz, $\gamma_{20} = 0.1$ MHz, $a = 2$ μm, and $\Omega_{\text{eff}} = 6$ MHz.

the 1/3 Talbot plane, the distinct focusing phenomena can be obtained at the 1/2 Talbot plane. As shown in Figure 6c3, all the bright spots in the six lattice sites evolve into the dark spots in the image, while the dark background in the regions immediately around the sites becomes bright honeycomb centers. Moreover, a phase shift of π occurs at the 1/2 Talbot length. This phenomenon is attributed to the fields from two nearest adjacent sites in the image overlapping completely, thus leading to constructive interference at the honeycomb centers and destructive interference at the six lattice sites. Finally, we can see from Figure 6c4 that the simulated image at the first Talbot plane is an exact replica of Figure 6c1.

Now, we turn attention to the diffraction patterns of honeycomb lattice under the scanning manners ii) and iii), respectively. As before, we first focus on the evolution of amplitude-type honeycomb lattice. In case of the scanning manner ii), with setting $z_0 = z_T/2$ and $z_1 = 3z_T/2$, we can see from **Figure 7**a1 that an altered Talbot "carpet" is produced. Different from Figure 6a1, the diffraction patterns are reduced gradually when D_2 moves along the diffraction direction z from $z_2 = 0$ to $z_2 = z_T$. In particular, the spatial transverse resolution of the corresponding diffraction patterns at $z_2 = 0$, $z_T/3$, $z_T/2$ and z_T are repeated with a period of 8, 5.6, 5, and 2 μm, respectively. On the other hand, different phenomena can be observed in manner iii). As shown in Figure 7a2, by setting $z_0 = z_T/4$ and $z_1 = z_T/2$, the diffraction patterns are changed from 6, 26, 10, to 4.66 μm if D_2 is located at $z_2 = 0$, $z_T/3$, $z_T/2$, and z_T, respectively. Therefore, the transverse resolution of diffraction patterns is decreased first and then increased when D_2 is scanning along the diffraction direction z.

These phenomena coincide well with the predictions made from Equation (7). First, $\Psi(u_1, u_1, v_1, v_1)$ is very sensitive to the change of the positions of the two detectors, and the diffraction patterns are magnified by a factor of $M_2 = |1 + z_1/(z_0+z_2)|$ ($M_3 = |1 + 2z_1/(z_0+z_2 - z_1)|$) in the ii) (iii)) scanning way. Therefore, if D_2 moves along the longitudinal direction, the transverse diffraction pattern gradually decreases in the second scanning method, while it increases first and then decreases in the third scanning method. Second, considering the second-order spatial correlation function $G^{(2)}(u_m, u_n)$, we find that the spatial resolution is closely dependent on the spatial correlation term $\text{Sinc}(\Delta\theta(u_m+u_n)/\lambda)$,[39] and the spatial resolution can be improved by a factor of 2 if we move the two single-photon detectors as the way in manner iii).

To quantitatively illustrate the role of the phase modulation on these images, we consider the hybrid-type honeycomb lattice, as shown in Figure 7b1,b2, where the parameters and scanning manners used are the same as those in Figure 7a1,a2, respectively, except $\Delta_1 = -\Delta_2 = 3$ MHz. It is apparent that not only the resolution of images, but also the location of Talbot plane is unchanged when the phase modulation is introduced (see also in Figure 7c1–c4 and Figure 7d1–d4), that is to say, those properties are independent of the phase modulation. However, a discrepancy can be found by careful comparing Figure 7a1,b1 (or Figure 7a2,b2), in which the maximum amplitude contrast decreases and the images under the amplitude-type honeycomb lattice are clearer than those of hybrid-type if the phase is introduced. All of these agree well with the predictions drawn from Equation (7).

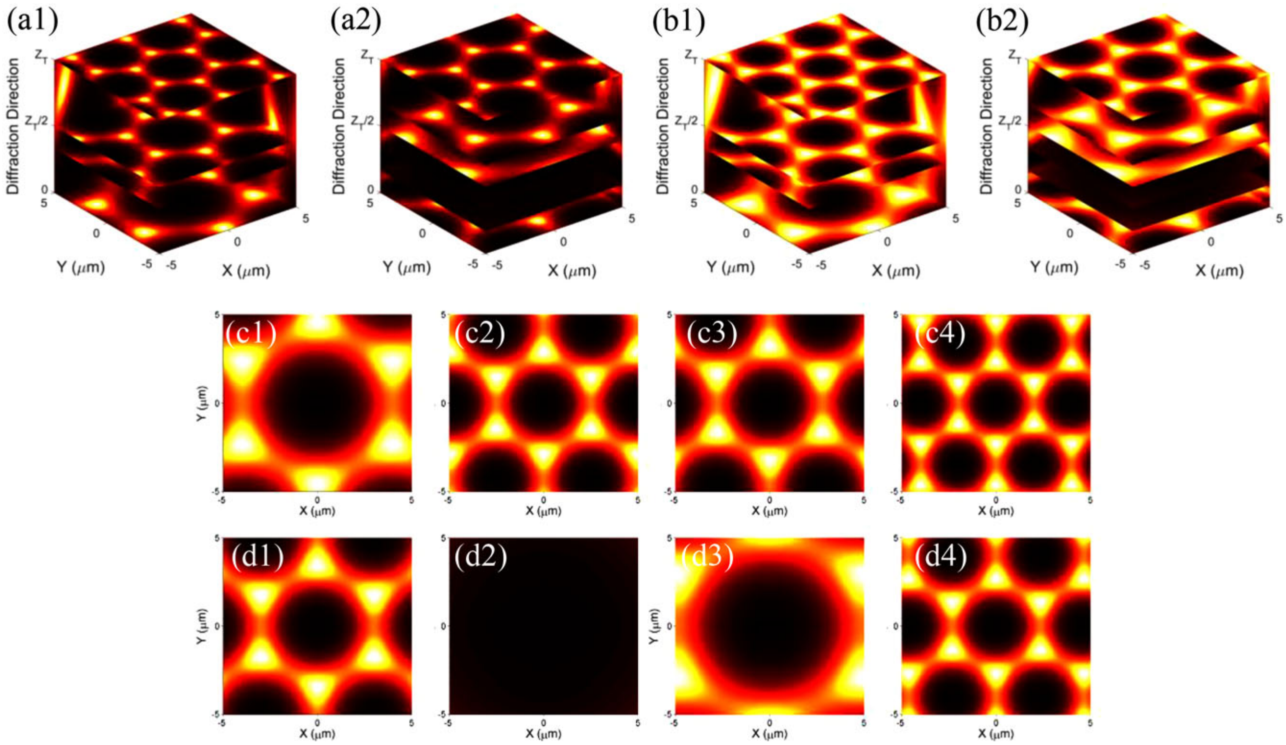

Figure 7. The near-field diffraction pattern of 2D honeycomb lattice along the z-direction obtained by scanning D_1 and D_2 in manner ii), with a1) $\Delta_1 = \Delta_2 = 0$ MHz and b1) $\Delta_1 = -\Delta_2 = 3$ MHz. The near-field diffraction pattern by scanning D_1 and D_2 in manner iii), with a2) $\Delta_1 = \Delta_2 = 0$ MHz and b2) $\Delta_1 = -\Delta_2 = 3$ MHz. The four panels in c) and in d) are the contour plots of b1) and b2) parallel to X-Y plane, at 0, $z_T/3$,$z_T/2$, and z_T, respectively. Other parameters are $\gamma_{10} = 1$ MHz, $\gamma_{20} = 0.1$ MHz, $a = 2$ μm, and $\Omega_{\text{eff}} = 6$ MHz.

Before summarizing this section, two points should be emphasized. First, assisted by small angle condition and two-photon Doppler-free technique,[40,41] the scheme proposed here can be implemented both in the cold and warm atomic vapor. Second, the transverse resolution of honeycomb lattices can be further increased via multiphoton entangled states.[42] Although the realization of multiphoton entangled source is experimentally challenging, the inherent physics would be of great richness and well worth studying.

4. Conclusions

In conclusion, assisted with multi-beam interference method, we have proposed a scheme for the construction of the honeycomb lattice in multi-level atomic vapor ensembles. We have illustrated how the absorption and dispersion properties of the formed lattice are modulated under different parameter conditions, and thus the generation of the amplitude/phase modulation honeycomb lattice. Furthermore, we exploit the diffraction pattern of the two typical lattices, and find that the transverse resolution of imaging is determined by the scanning manner of two detectors. In addition, we also indicate that the optical properties of the induced lattice are associated with the imaging contrast. The further development of our proposal will be presented in 2D atom super-resolution optical testing, all-optical switching at the few photons level, and can be used for the generation and manipulation of optical topological insulators as well.

Supporting Information

Supporting Information is available from the Wiley Online Library or from the author.

Acknowledgements

F.W. and H.Y. contributed equally to this work. We acknowledge helpful discussions with Prof. Yi. Qi. Zhang. This work is financially supported by the National Natural Science Foundation of China (61605155, and 61627812), the Fundamental Research Funds for the Central Universities, and the National Key R&D Program of China (2017YFA0303700). Feng Wen is partly supported by the 2016 International Postdoctoral Exchange Fellowship Program of the Office of the China Postdoctoral Council. Zhiping Dai acknowledges the support by the Scientific Research Fund of Hunan Provincial Education Department (Grant No. 17B038).

Conflict of Interest

The authors declare no conflict of interest.

Keywords

artificial periodic structures, honeycomb lattice, near-field diffraction

Received: February 13, 2018
Revised: May 9, 2018
Published online: June 10, 2018

[1] H. Eisenberg, Y. Silberberg, R. Morandotti, A. Boyd, J. Aitchison, *Phys. Rev. Lett*. **1998**, *81*, 3383.
[2] D. N. Christodoulides, F. Lederer, Y. Silberberg, *Nature* **2003**, *424*, 817.
[3] H.-G. Park, S.-H. Kim, S.-H. Kwon, Y.-G. Ju, J.-K. Yang, J.-H. Baek, S.-B. Kim, Y.-H. Lee, *Science* **2004**, *305*, 1444.
[4] Y. Akahane, T. Asano, B.-S. Song, S. Noda, *Nature* **2003**, *425*, 944.
[5] J. D. Joannopoulos, S. G. Johnson, J. N. Winn, R. D. Meade, *Photonic Crystals: Molding the Flow of Light*, Princeton University Press, USA **2011**.
[6] D. R. Smith, J. B. Pendry, M. C. Wiltshire, *Science* **2004**, *305*, 788.
[7] T. Han, X. Bai, J. T. Thong, B. Li, C. W. Qiu, *Adv. Mater*. **2014**, *26*, 1731.
[8] T. Baba, *Nat. Photonics* **2008**, *2*, 465.
[9] P. Lodahl, A. F. Van Driel, I. S. Nikolaev, A. Irman, K. Overgaag, D. Vanmaekelbergh, W. L. Vos, *Nature* **2004**, *430*, 654.
[10] P. Longo, P. Schmitteckert, K. Busch, *Phys. Rev. Lett*. **2010**, *104*, 023602.
[11] Y. Yang, G. Thirunavukkarasu, M. Babiker, J. Yuan, *Phys. Rev. Lett*. **2017**, *119*, 094802.
[12] Y. Yang, Y. Dong, C. Zhao, Y. Cai, *Opt. Lett*. **2013**, *38*, 5418.
[13] D. Gao, W. Ding, M. Nieto-Vesperinas, X. Ding, M. Rahman, T. Zhang, C. Lim, C.-W. Qiu, *Light Sci. Appl*. **2017**, *6*, e17039.
[14] C.-W. Qiu, W. Ding, M. Mahdy, D. Gao, T. Zhang, F. C. Cheong, A. Dogariu, Z. Wang, C. T. Lim, *Light Sci. Appl*. **2015**, *4*, e278.
[15] A. Alù, N. Engheta, *Phys. Rev. Lett*. **2009**, *103*, 143902.
[16] Y. He, Y. Li, J. Liu, X. Zhang, Y. Cai, Y. Chen, S. Chen, D. Fan, *Sci. Rep*. **2017**, *7*, 6814.
[17] Z. Dai, Z. Yang, X. Ling, S. Zhang, Z. Pang, X. Li, Y. Wang, *Sci. Rep*. **2017**, *7*, 122.
[18] O. Bahat-Treidel, O. Peleg, M. Grobman, N. Shapira, M. Segev, T. Pereg-Barnea, *Phys. Rev. Lett*. **2010**, *104*, 063901.
[19] M. C. Rechtsman, Y. Plotnik, J. M. Zeuner, D. Song, Z. Chen, A. Szameit, M. Segev, *Phys. Rev. Lett*. **2013**, *111*, 103901.
[20] L. Chen, C.-C. Liu, B. Feng, X. He, P. Cheng, Z. Ding, S. Meng, Y. Yao, K. Wu, *Phys. Rev. Lett*. **2012**, *109*, 056804.
[21] Y. Zhang, Y. V. Kartashov, F. Li, Z. Zhang, Y. Zhang, M. R. Belic, M. Xiao, *ACS Photonics* **2017**, *4*, 2250.
[22] Y. Zhang, Z. Wu, M. R. Belić, H. Zheng, Z. Wang, M. Xiao, Y. Zhang, *Laser Photonics Rev*. **2015**, *9*, 331.
[23] A. Singha, M. Gibertini, B. Karmakar, S. Yuan, M. Polini, G. Vignale, M. I. Katsnelson, A. Pinczuk, L. N. Pfeiffer, K. W. West, V. Pellegrini, *Science* **2011**, *332*, 1176.
[24] D. Song, V. Paltoglou, S. Liu, Y. Zhu, D. Gallardo, L. Tang, J. Xu, M. Ablowitz, N. K. Efremidis, Z. Chen, *Nat. Commun*. **2015**, *6*, 6272.
[25] M. Greiner, S. Fölling, *Nature* **2008**, *453*, 736.
[26] S. Kubo, Z.-Z. Gu, K. Takahashi, A. Fujishima, H. Segawa, O. Sato, *J. Am. Chem. Soc*. **2004**, *126*, 8314.
[27] S. F. Mingaleev, Y. S. Kivshar, *Phys. Rev. Lett*. **2001**, *86*, 5474.
[28] M. Mitsunaga, N. Imoto, *Phys. Rev. A*. **1999**, *59*, 4773.
[29] A. W. Brown, M. Xiao, *Opt. Lett*. **2005**, *30*, 699.
[30] A. Andre, M. Lukin, *Phys. Rev. Lett*. **2002**, *89*, 143602.
[31] F. Wen, H. Ye, X. Zhang, W. Wang, S. Li, H. Wang, Y. Zhang, C.-W. Qiu, *Photon. Res*. **2017**, *5*, 676.
[32] D. A. Steck, http://steck.us/alkalidata **2012**.
[33] M. O. Scully, M. S. Zubairy, *Quantum Optics*, Cambridge University Press, UK **1999**.
[34] R. J. Glauber, *Quantum Theory of Optical Coherence: Selected Papers and Lectures*, John Wiley & Sons, USA **2007**.
[35] F. Wen, W. Wang, I. Ahmed, H. Wang, Y. Zhang, Y. Zhang, A. R. Mahesar, M. Xiao, *Sci. Rep*. **2017**, *7*, 41790.
[36] F. Shen, A. Wang, *Appl. Optics* **2006**, *45*, 1102.
[37] H. Ye, C. Qiu, K. Huang, J. Teng, B. Luk'yanchuk, S. P. Yeo, *Laser Phys. Lett*. **2013**, *10*, 065004.
[38] M. Gu, *Advanced Optical Imaging Theory*, Springer Science & Business Media, Germany **2000**.
[39] F. Wen, X. Zhang, C. Yuan, H. Zheng, X. Yao, Z. Li, Y. Zhang, *J. Phys. B* **2015**, *48*, 075401.
[40] Y. Li, M. Xiao, *Phys. Rev. A* **1995**, *51*, 4959.
[41] Y. Zhang, Z. Wang, Z. Nie, C. Li, H. Chen, K. Lu, M. Xiao, *Phys. Rev. Lett*. **2011**, *106*, 093904.
[42] M. W. Mitchell, J. S. Lundeen, A. M. Steinberg, *Nature* **2004**, *429*, 161.